Modeling of Small Fatigue Cracks in Low SFE Microstructures

Subcontract from QuesTek LLC from Bechtel/Bettis Prime
Program Manager and Technical Monitor at QuesTek LLC: Dr. J. Sebastian

Georgia Tech PI/PD
David L. McDowell, Regents' Professor
GWW School of Mechanical Engineering, Georgia Institute of Technology
4105 MRDC, 801 Ferst Dr., Atlanta, GA 30332-0405
david.mcdowell@me.gatech.edu, Ph: 404-894-5128, Fax: 404-894-0186

Post Doc: Jagan Padbidri
PhD Student: Matthew Priddy (08/2010 – 12/2010)

Introduction

Nuclear reactor pressure vessels are manufactured from high strength steels like A302B. The inner surface of the pressure vessel is exposed to extremely corrosive environments at high temperatures. The pressure vessels are therefore clad with corrosion resistant materials such as austenitic stainless steel. However, the manufacturing process results in defects in the clad material and the clad/base material interface. These defects are subject to fatigue loading due to the pressurization/shutdown cycles of the pressure vessel during service resulting in fatigue crack formation and growth from the defects. Here, we focus on the formation and growth of a fatigue crack from a surface defect in the cladding material to the base metal that could lead to exposure of the base metal to the corrosive environment in the pressure vessel and subsequent failure.

To quantify the crack propagation rate from these defects under cyclic loading conditions, a Short crack growth (ShCGr) model has been developed by Dr. Clint Geller of the Bettis Atomic Power Laboratory (BAPL). The ShCGr model employs the concept of an accumulating debris field associated with the irreversibility attributed to dislocations encountering obstacles to their motion over a number of loading cycles; this contributes to stress intensification at the crack tip. The model uses an irreversibility factor to account for the damage accumulation. The number of cycles required for crack extension is found from energy balance between the free energy change associated with creating a crack and the energy released by a dislocation pile-up when a crack is created. The model is able to correlate crack initiation lives in smooth specimens through certain assumptions.

The model also attempts to capture the credit for the cycles required to incubate the crack growth process up until the point at which steady state (i.e., Paris growth law behavior) is realized. This is described as the process of "conditioning" the state of cyclic plastic deformation in the process zone to a point where crack extension can occur. An hypothesis to be explored is that the a full description of this "conditioning" process can lead to the realization of a "credit" of fatigue cycles relative to application of the Paris growth law for propagation treating the initial defect as a crack. Realization of such a "credit" could have extremely important implications for nuclear reactor pressure vessel maintenance schedules and procedures and could provide a basis for extending useful service lifetime. In its current form, the foundational elements of the ShCGr model have a sound basis. However, there are certain key elements that require either experimental calibration or numerical modeling strategies to establish reliable functional forms.

This research program at Georgia Tech has been subcontracted from QuesTek LLC with Bettis Atomic Power Lab (BAPL) as prime. The objective of the research is to develop crystal plasticity-based computational methods to model fatigue crack initiation in cladding materials (SS 308). The research conducted in this program is intended to augment and provide input into the Short Crack Growth (ShCGr) model developed by Dr. Clint Geller (BAPL) and enhance its predictive capabilities. A key outcome of the Phase I (2009) effort was the understanding of the ShCGr model and strategies to enhance its capabilities. The present Phase II research program commenced on 8/1/10. The overall Gantt chart for the entire Phase II program is shown in Figure 1.

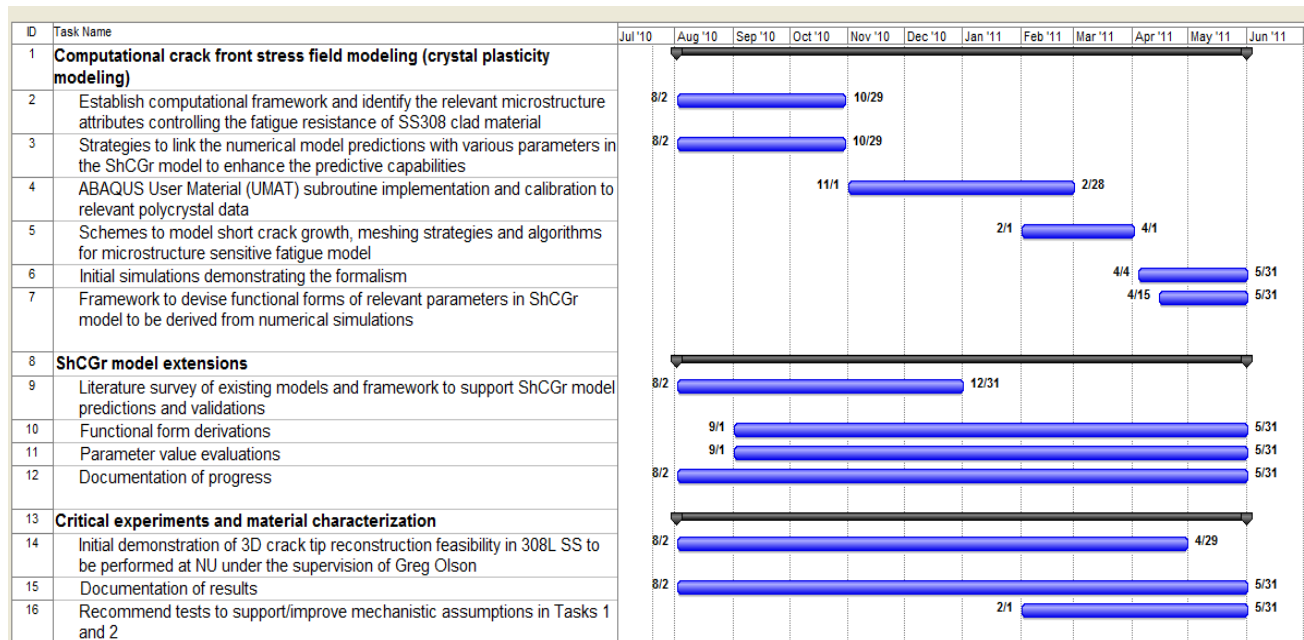| ID	Task Name	Jul '10	Aug '10	Sep '10	Oct '10	Nov '10	Dec '10	Jan '11	Feb '11	Mar '11	Apr '11	May '11	Jun '11
1	**Computational crack front stress field modeling (crystal plasticity modeling)**												
2	Establish computational framework and identify the relevant microstructure attributes controlling the fatigue resistance of SS308 clad material		8/2 ▬▬▬ 10/29										
3	Strategies to link the numerical model predictions with various parameters in the ShCGr model to enhance the predictive capabilities		8/2 ▬▬▬ 10/29										
4	ABAQUS User Material (UMAT) subroutine implementation and calibration to relevant polycrystal data					11/1 ▬▬▬			2/28				
5	Schemes to model short crack growth, meshing strategies and algorithms for microstructure sensitive fatigue model								2/1 ▬▬ 4/1				
6	Initial simulations demonstrating the formalism										4/4 ▬▬ 5/31		
7	Framework to devise functional forms of relevant parameters in ShCGr model to be derived from numerical simulations										4/15 ▬▬ 5/31		
8	**ShCGr model extensions**												
9	Literature survey of existing models and framework to support ShCGr model predictions and validations		8/2 ▬▬▬▬▬ 12/31										
10	Functional form derivations			9/1 ▬▬▬▬▬▬▬▬▬ 5/31									
11	Parameter value evaluations			9/1 ▬▬▬▬▬▬▬▬▬ 5/31									
12	Documentation of progress		8/2 ▬▬▬▬▬▬▬▬▬▬ 5/31										
13	**Critical experiments and material characterization**												
14	Initial demonstration of 3D crack tip reconstruction feasibility in 308L SS to be performed at NU under the supervision of Greg Olson		8/2 ▬▬▬▬▬▬▬▬ 4/29										
15	Documentation of results		8/2 ▬▬▬▬▬▬▬▬▬▬ 5/31										
16	Recommend tests to support/improve mechanistic assumptions in Tasks 1 and 2								2/1 ▬▬▬▬ 5/31				

Figure 1: Project Gantt chart of the 10 months Phase II program (Year 1 of a multi-year Phase II program).

As in the original proposal, the GT effort has addressed the following tasks in the first year:

- Worked with QuesTek to fit a limited slip crystal plasticity model suitable for description of cyclic plastic straining of low stacking fault energy alloys of relevance to cladding applications, with top-down parameter estimation from experimental data. An ABAQUS [1] User Material Subroutine (UMAT) was developed for this purpose to model single and polycrystalline behavior.
- Meshes for polycrystals with realistic grain size/secondary dendrite cell size distribution were developed for notch root radii of relevance to initial defects in claddings, in the range of tens to hundreds of microns. Input from QuesTek guided consideration of dendritic structure in meshing, include orientation of primary dendrites.
- An initial crystal plasticity-based model was developed to assess driving forces for Stage I crystallographic cracks, including cracks embedded in homogeneous planar slip regions and cracks growing at the interface of the matrix and slip bands. Algorithms were established for estimating local crack tip driving forces as a function of notch depth and root radius to grain diameter. These models will be applied later in the program to estimate crack growth rates for

crack expansion in a field of grains with size and orientation distribution in the small crack growth regime prior to attaining conditions of similitude characteristic of a fully developed crack front.
- Exercised the polycrystalline model for various applied stress amplitudes and R-ratios (mean stress) to quantify the distribution of slip and average notch root stress shielding effects.
- Relevance of these tools and studies to informing elements of the ShCGr model were expanded upon and clarified.

1. Problem Description

The problem of interest is the formation and early growth of cracks from surface defects occurring in cladding materials subjected to fatigue loading as the pressure vessel undergoes pressurization/shutdown cycles. The defects occur on the surface of the cladding material, with the crack forming and propagating into the cladding material. The focus is on the role of clad microstructure in the development of cyclic plasticity around the deep notch root that drives formation and early growth of a fatigue crack into the cladding material. This study is intended to characterize the stress distribution in the vicinity of the notch for different notch root radii and remote stress loading amplitudes. Also of primary interest is the distribution of slip in the microstructure around the notch root which drives fatigue crack formation and early growth.

To this end, a computational model along the lines of that shown in Figure 2 has been developed based on decomposing the volume around the notch into several regimes with different constitutive laws. The immediate vicinity of the notch is modeled as an explicit ensemble of grains or dendrite cells using crystal plasticity. This innermost region is surrounded by a regime described by nonlinear kinematic hardening plasticity beyond which linear elasticity is used. The constitutive relations for each regime are addressed next.
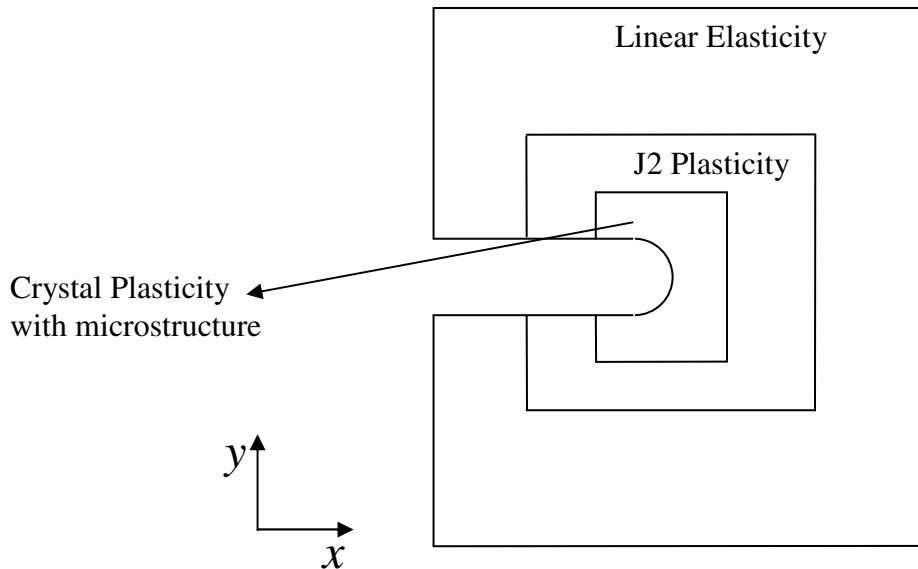
Figure 2: Domain decomposition in the vicinity of the notch (not to scale).

2. Domain Decomposition: Constitutive Relations

2.1 Crystal Plasticity

The primary vehicle to simulate the formation of small cracks at the notch tip and analyze the driving forces associated with the crack growth is crystal plasticity. The material in question is austenitic steel with FCC crystal structure with 12 possible octahedral slip systems. The shearing rate of a slip system is described by a power law as

$$\dot{\gamma}^{\alpha} = \dot{\gamma}_0 \left(\frac{\left\langle \tau^{\alpha} - \chi^{\alpha} \right\rangle - \kappa^{\alpha}}{g^{\alpha}} \right)^m \operatorname{sgn}\left(\tau^{\alpha} - \chi^{\alpha} \right) \tag{1}$$

where $\dot{\gamma}^{\alpha}$ is the shearing rate on slip system α, $\dot{\gamma}_0$ is the reference shearing rate, χ^{α} is the back stress on slip system α, g^{α} is the drag stress, κ^{α} is the threshold stress, m is the inverse strain rate sensitivity exponent, and τ^{α} is the resolved shear stress on slip system α. Here, $\left\langle \tau^{\alpha} - \chi^{\alpha} \right\rangle = \left(\tau^{\alpha} - \chi^{\alpha} \right) u \left(\tau^{\alpha} - \chi^{\alpha} \right)$ is the Macauley bracket function of overstress.

For austenitic steels, the threshold stress is important in terms of isotropic hardening, and evolves according to a hardening versus dynamic recovery format [1], i.e.,

$$\dot{\kappa}^{\alpha} = A \sum_{\beta=1}^{n} h_{\alpha\beta} \left| \dot{\gamma}^{\beta} \right| - B \, \kappa^{\alpha} \sum_{\beta=1}^{n} \left| \dot{\gamma}^{\beta} \right| \tag{2}$$

Here, A and B are the direct hardening and dynamic recovery coefficients and $h_{\alpha\beta}$ represents the hardening matrix, with $h_{\alpha\alpha}$ representing self-hardening and $h_{\alpha\beta}, \alpha \neq \beta$ representing latent hardening.

The evolution of the slip system back stress is given by a nonlinear kinematic hardening rule [2, 3] of the Armstrong–Frederick self-hardening form, i.e.,

$$\dot{\chi}^{\alpha} = C \dot{\gamma}^{\alpha} - D \chi^{\alpha} \left| \dot{\gamma}^{\alpha} \right| \tag{3}$$

where C and D are the direct hardening and dynamic recovery coefficients, respectively.

2.2 Elastic-Plastic Zone

The crystal plasticity zone is surrounded by an elastic-plastic material with a yield function given by

$$F = \frac{3}{2} (\mathbf{S} - \boldsymbol{\chi}') : (\mathbf{S} - \boldsymbol{\chi}') - \sigma_y^2 = 0 \tag{4}$$

Here, $\mathbf{S}$ is the deviatoric part of the stress tensor, χ' is the deviatoric part of the back stress tensor, and σ_y is the uniaxial yield strength of the material. A nonlinear kinematic hardening law [4] is used to describe the evolution of the back stress tensor, i.e.,

$$\dot{\chi} = \frac{c}{\sigma_y}(\boldsymbol{\sigma} - \boldsymbol{\chi})\dot{\bar{\varepsilon}}_{pl} - \gamma\chi\dot{\bar{\varepsilon}}_{pl} \tag{5}$$

where c and γ are material parameters to be calibrated, and $\dot{\bar{\varepsilon}}_{pl}$ is the rate of evolution of the equivalent plastic strain, given by

$$\dot{\bar{\varepsilon}}_{pl} = \sqrt{\frac{2}{3}\dot{\boldsymbol{\varepsilon}}_{pl} : \dot{\boldsymbol{\varepsilon}}_{pl}} \tag{6}$$

Since the hardening law used for the continuum description of the material is purely kinematic, the cyclic stress-strain response will be stable. The material parameters used in the nonlinear kinematic hardening law in Equation (5) is calibrated to cyclic stress-strain data provided by QuesTek at the temperature(s) and strain rate(s) of interest.

3. Considerations for Modeling
3.1 Stable Hysteresis

Stainless steel 308 exhibits transient hardening during the first half of fatigue life [5] as shown in Figure 3 for completely reversed (R=-1) loading. The majority of proposed simulations will make use of the stable half life hysteresis response, i.e., the cyclically stable stress-strain curve, ignoring transient isotropic hardening.

(a)
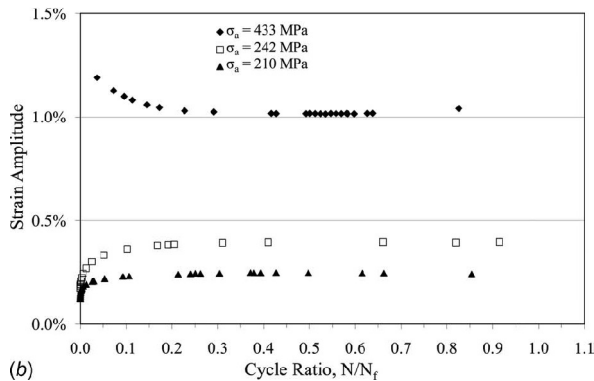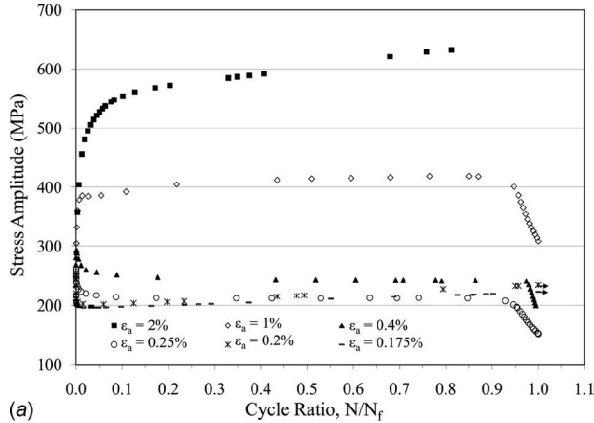
Figure 3: (a) Stress responses from strain-controlled fatigue tests and (b) strain responses from load-controlled fatigue tests versus number of cycles for stainless steel 304L [5].

(b)

5

The influence of isotropic hardening transients will be considered in selected simulations to consider the approximation error incurred due to this assumption.

3.2 Planar Slip

An additional consideration is that the cladding material (SS 308) is a low stacking fault energy material which exhibits planar slip [6]. Secondary slip is observed in some cases for these materials [7], and is primarily restricted to interfaces such as grain boundaries to account for compatibility with the neighbouring grains and also with the δ-Ferrite at the grain boundaries, as shown in Figure 4 (from Ref. [7]). This clearly suggests that the interior of the grain has fewer active slip systems than regions near the grain boundary and that the distance from the grain boundary should be used as a basis for assigning the maximum number of active slip systems at a spatial point in a grain.
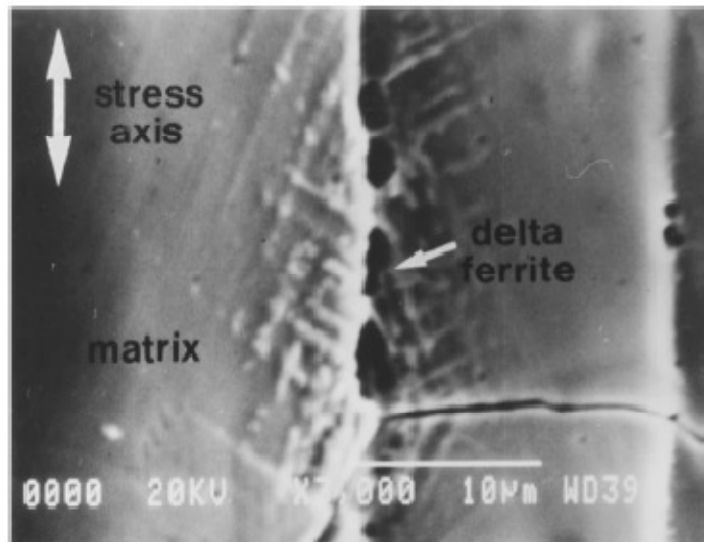
Figure 4: Scanning electron micrographs showing the slip pattern near the interface between the matrix and δ-ferrite. Both primary and secondary slip are shown, and the secondary slip was explained by strain incompatibility (from Ref. [7]).

We will consider mainly primary slip with perhaps 1-2 active secondary systems at the relatively low strain amplitudes relevant to fatigue. This can be achieved by specifically constraining the slip on all the systems other than the slip on a few initially activated systems based on the local (actual) Schmid factor acting on these slip systems. The algorithm for constrained slip was developed by Lloyd [8]. The premise of the algorithm is to limit the maximum number of active slip systems based on the distance from the grain boundary with regions near the grain boundary – "mantle", being allowed more active slip systems than the interior – "core". A schematic of the mantle – core approach is shown in Figure 5. It is to be noted that the elastic properties of the mantle and core of a grain are the same and they differ only in the number of active slip systems. Based on Figure 4, it can be observed that the regions that are about 5μm from the grain boundaries form the mantle of a grain and the rest is the core. The implementation of identifying the mantle and core of a grain will be elaborated later.
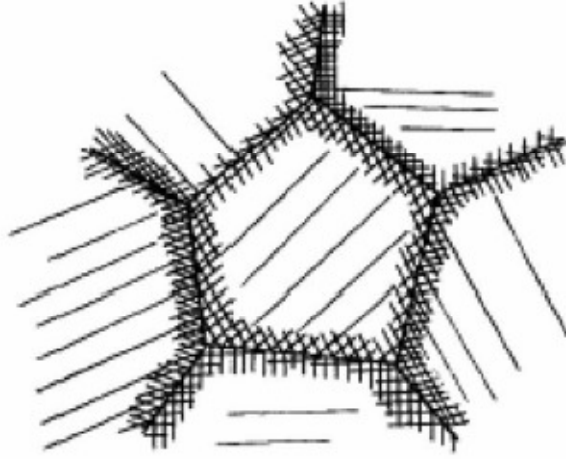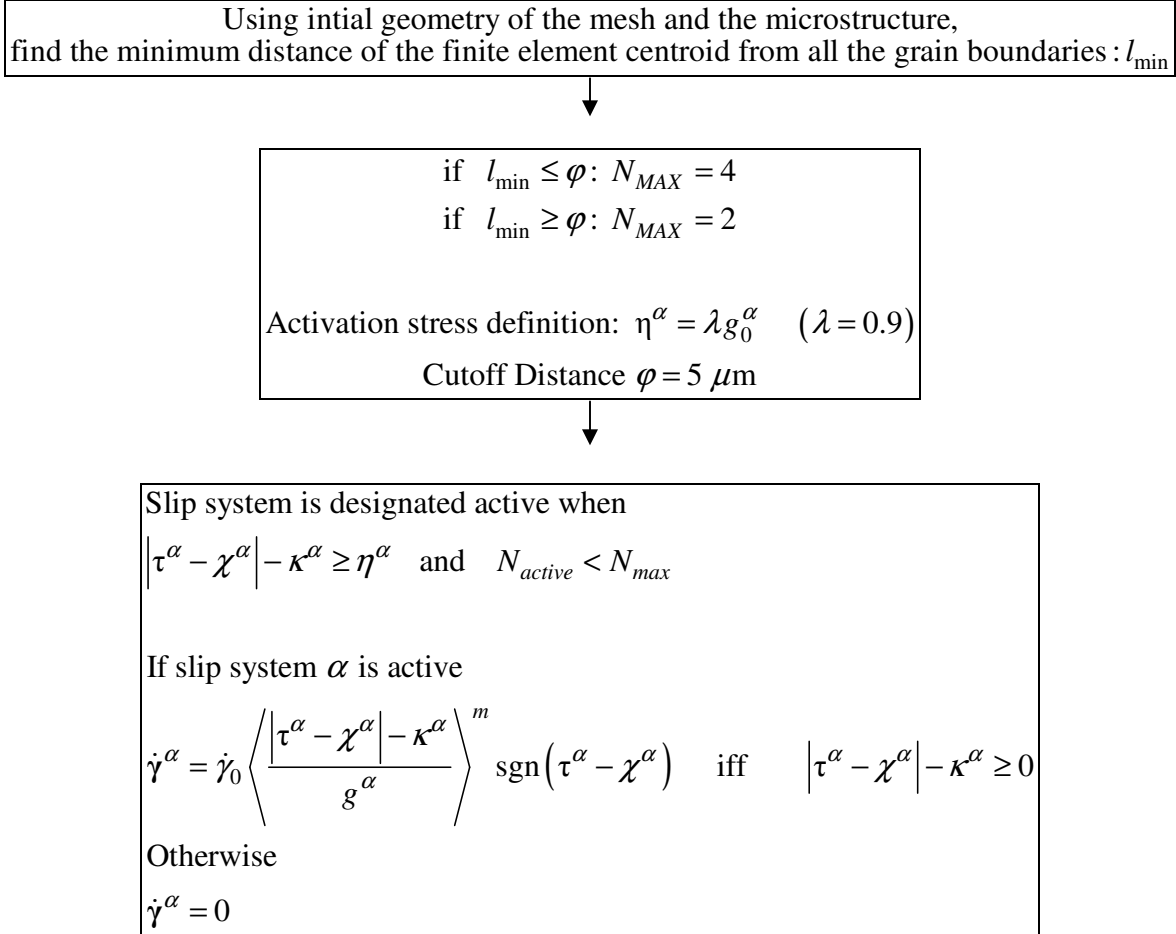
Figure 5: Mantle-Core model showing limited slip on the interior section, and multiple slip near the grain boundary (from Ref. [9]).

The algorithm used here is a slight modification of that proposed by Lloyd [8]. While Lloyd prescribes an inflated drag stress to reduce the slip rates on the inactive slip systems, we explicitly nullify it. A flowchart of the algorithm used is shown below. The algorithm is implemented as a user material (UMAT) in ABAQUS [4] with modifications from Lloyd [8].

Using intial geometry of the mesh and the microstructure, find the minimum distance of the finite element centroid from all the grain boundaries : l_{min}

if $l_{min} \leq \varphi$: $N_{MAX} = 4$

if $l_{min} \geq \varphi$: $N_{MAX} = 2$

Activation stress definition: $\eta^\alpha = \lambda g_0^\alpha$ $(\lambda = 0.9)$

Cutoff Distance $\varphi = 5 \, \mu m$

Slip system is designated active when

$\left| \tau^\alpha - \chi^\alpha \right| - \kappa^\alpha \geq \eta^\alpha$ and $N_{active} < N_{max}$

If slip system α is active

$$\dot{\gamma}^\alpha = \dot{\gamma}_0 \left\langle \frac{\left| \tau^\alpha - \chi^\alpha \right| - \kappa^\alpha}{g^\alpha} \right\rangle^m \operatorname{sgn}\left(\tau^\alpha - \chi^\alpha \right) \quad \text{iff} \quad \left| \tau^\alpha - \chi^\alpha \right| - \kappa^\alpha \geq 0$$

Otherwise

$\dot{\gamma}^\alpha = 0$

Here, N_{max} is the number of allowable activated slip systems (4 for mantle, 2 for core) and N_{active} is the number of active slip systems which is updated when a new slip system activates. It is to be noted that this approach will be consistent in the calibration studies performed using 3D finite element meshes.

3.3 Viscoplastic Behavior

The material under consideration, SS 304, exhibits significant time-dependent properties (strain rate sensitivity and creep) at both room temperature and elevated temperatures. Krempl [10] performed rate-sensitive creep tests on SS 304 at room temperature. The strain rates ranges from 1×10^{-8} to 1×10^{-2} s^{-1}. A uniaxial stress-strain curve of three different tests with two of the tests changing the strain rate by three orders of magnitude instantaneously during the test is shown in Figure 6. Figure 7 is a unaxial stress-strain curve depicting SS 304 undergoing cyclic creep at room temperature. Kujawski [11] studied the influence of uniaxial strain on subsequent creep in SS 304 at room temperature. Figure 8 is a stress-strain curve of uniaxial loading with subsequent creep tests (holds) performed at three increasing stress levels.

FIG. 2. Stress-strain diagrams at different strain-rates. At points A the strain-rate is instantaneously changed. Annealed AISI Type 304 stainless steel.
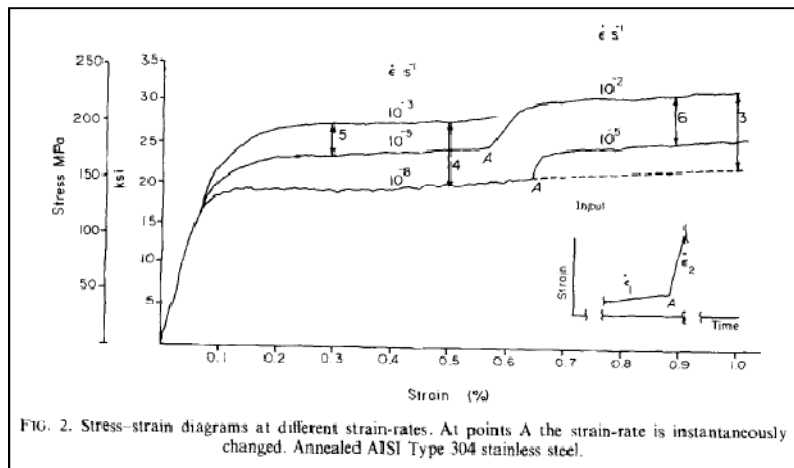
Figure 6: Three tensile tests at varying strain rates (10^{-2} to 10^{-8} s^{-1}) [10].

FIG. 8. Cyclic creep of a prestrained specimen. Creep periods of 60 s are followed by load cycling. Note the decrease in "ratchet strain" with cycles.
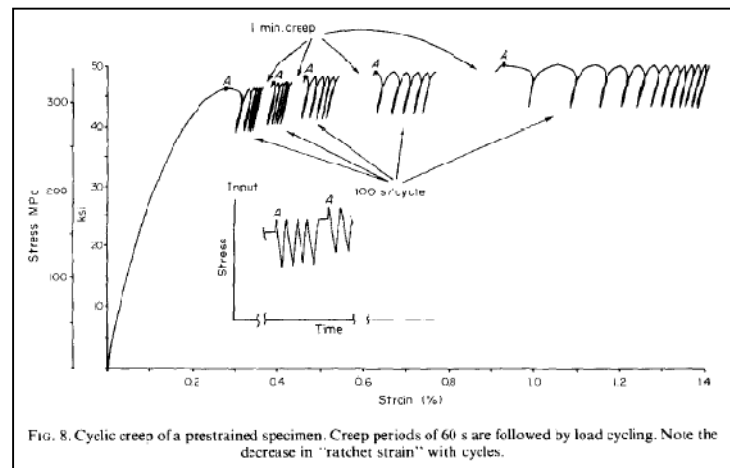
Figure 7: Cyclic creep of a specimen with prior mechanical history [10].

8

It can be concluded from the previous figures that SS 304 shows considerable positive strain rate sensitivity (stress increases with strain rate) at room temperature. As addressed earlier the majority of the simulations will be conducted using half-life response as representative of the cyclically stable stress-strain behavior. Figure 9 depicts the stabilized hysteresis response of SS 304 at two different strain rates from experiments by Krempl [10]. He conducted cyclic straining of the specimen subjected to both constant strain rates and strain rate jump tests during cyclic straining. It was observed that the stress jump when the strain rate was changed decreased with the number of cycles. Also, Moosbrugger [12] demonstrated that the overstress of SS 304 does not change appreciably as cyclic hardening occurs during cycling. This implies that the material undergoes a very complex hardening phenomenon. The parameters for the crystal viscoplasticity are estimated based on this behavior (Figs 6 and 9).

FIG. 2. Influence of stress-rate on subsequent creep behavior. Creep tests are performed at three different stress levels (Arabic numeral subscripts denote the stress level) using constant stress-rate loading between the stress levels.
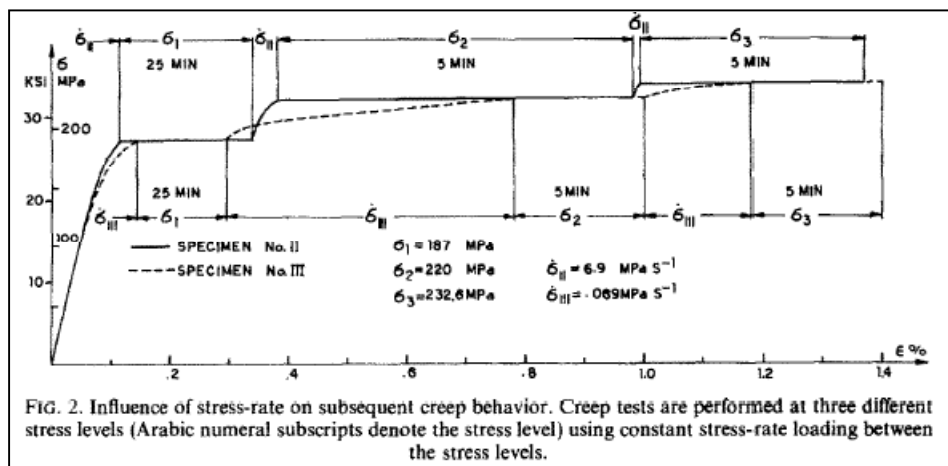
Figure 8: Effects of uniaxial prestrain on subsequent creep in 304SS (creep-plasticity interaction) [11].

FIG. 7. Steady-state hysteresis loops at strain-rates of 10^{-5} and 10^{-3} s^{-1}. Note that the two loops almost coincide during the unloading portion. At points D the strain-rates were changed. The transition from one to the other hysteresis loop is fully reversible. Continuation of test in Fig. 6.
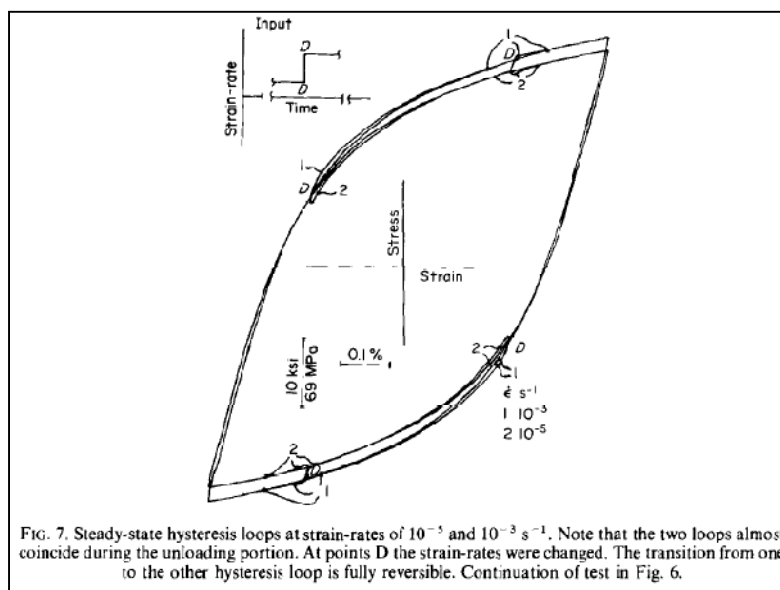
Figure 9: Cyclically stable stress-strain curves at different strain rates (10^{-3} and 10^{-5} s^{-1}) [10].

9

4 Calibration studies

4.1 Calibration of J2 plasticity parameters

The constitutive relations describing the elastic-plastic zone follow a nonlinear kinematic hardening rule (5) with an isotropic yield function (4). The parameters of the hardening rule need to be estimated to fit the material response at the temperature of interest. Since the plasticity is largely confined to the crystal plasticity zone, a rate independent constitutive model is being followed. The purpose of the J2 zone is to avoid a strong jump discontinuity of tangent stiffness mismatch between the crystal plasticity and the linear elastic zones. Estimation of the J2 parameters requires cyclically stable stress-strain curves at different amplitudes. Experiments by Leax [13] provide this data at the operating temperature (288°C), as shown in Figure 10.
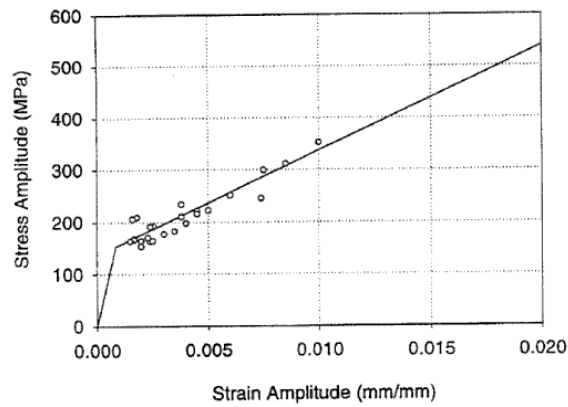
Figure 10: Cyclically stable stress-strain curve (288°C) [13].

The data in Figure 10 show the amplitudes of stress and strain at the temperature of interest. A power law relation between the stress and plastic strain ampliudes can be deduced (Figure 11) by partitioning the total strain amplitude into elastic and plastic parts.
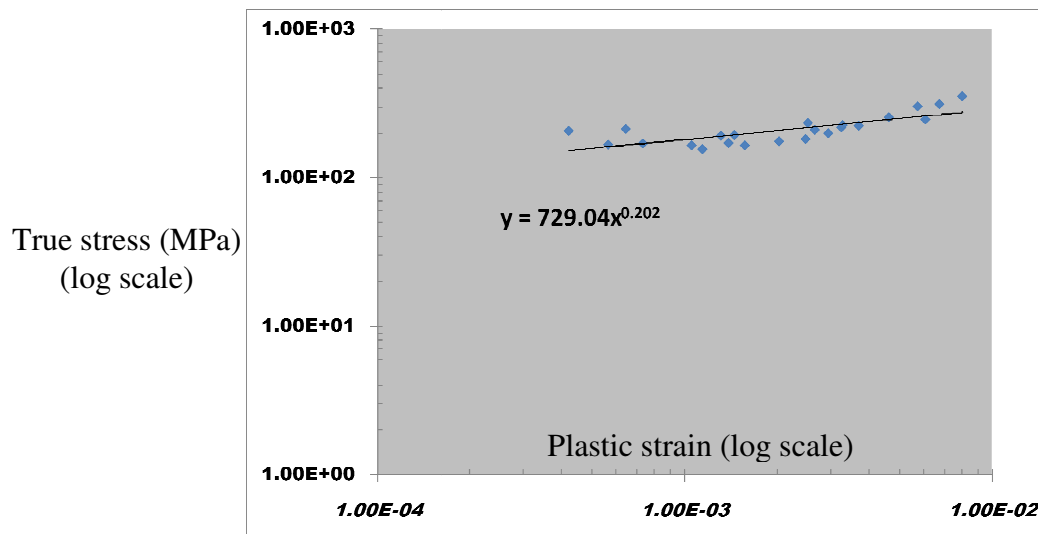
Figure 11: Power law relation between the plastic strain and stress amplitudes (288°C).

The simulation cell (cube) used for the calibrations contains 64 finite elements subjected to fully reversed strain cycles and random periodic boundary conditions using ABAQUS [4]. The response of the simulation cell is compared with the hysteresis curves obtained using data from Leax [13], as shown in Figure 12.
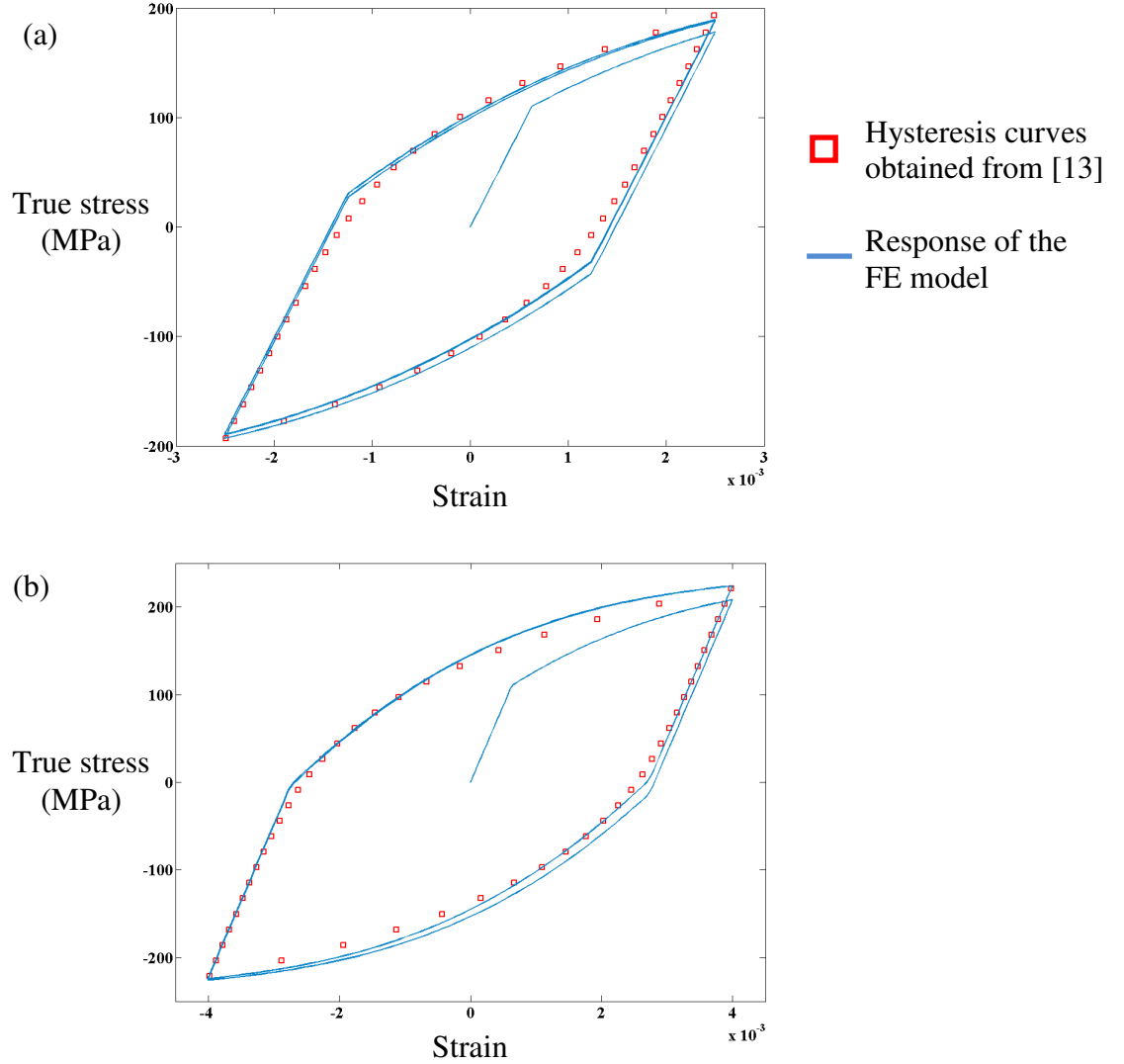
Figure 12: Calibration simulations for J2 plasticity. 3 completely reversed strain cycles with strain amplitudes of (a) 0.25% and (b) 0.4%.

The following values were obtained from the calibration studies:

$\sigma_y = 110$ MPa, $c = 65000$ MPa, $r = 500$

4.2 Calibration of Crystal plasticity parameters

The crystal plasticity model should capture the effect of the rate sensitivity. Calibration tests for parameter estimation were conducted based on data from Krempl [10], who performed rate sensitivity experiments at room temperature. Single strain rate and strain rate jump tests were conducted on a 1000 element, 50 grain 3D mesh with random periodic boundary conditions that takes into account the mantle – core zone distribution. The average values of overstress of all the active slip systems have also been listed. The results for uniaxial tensile tests are shown in Figure 13.
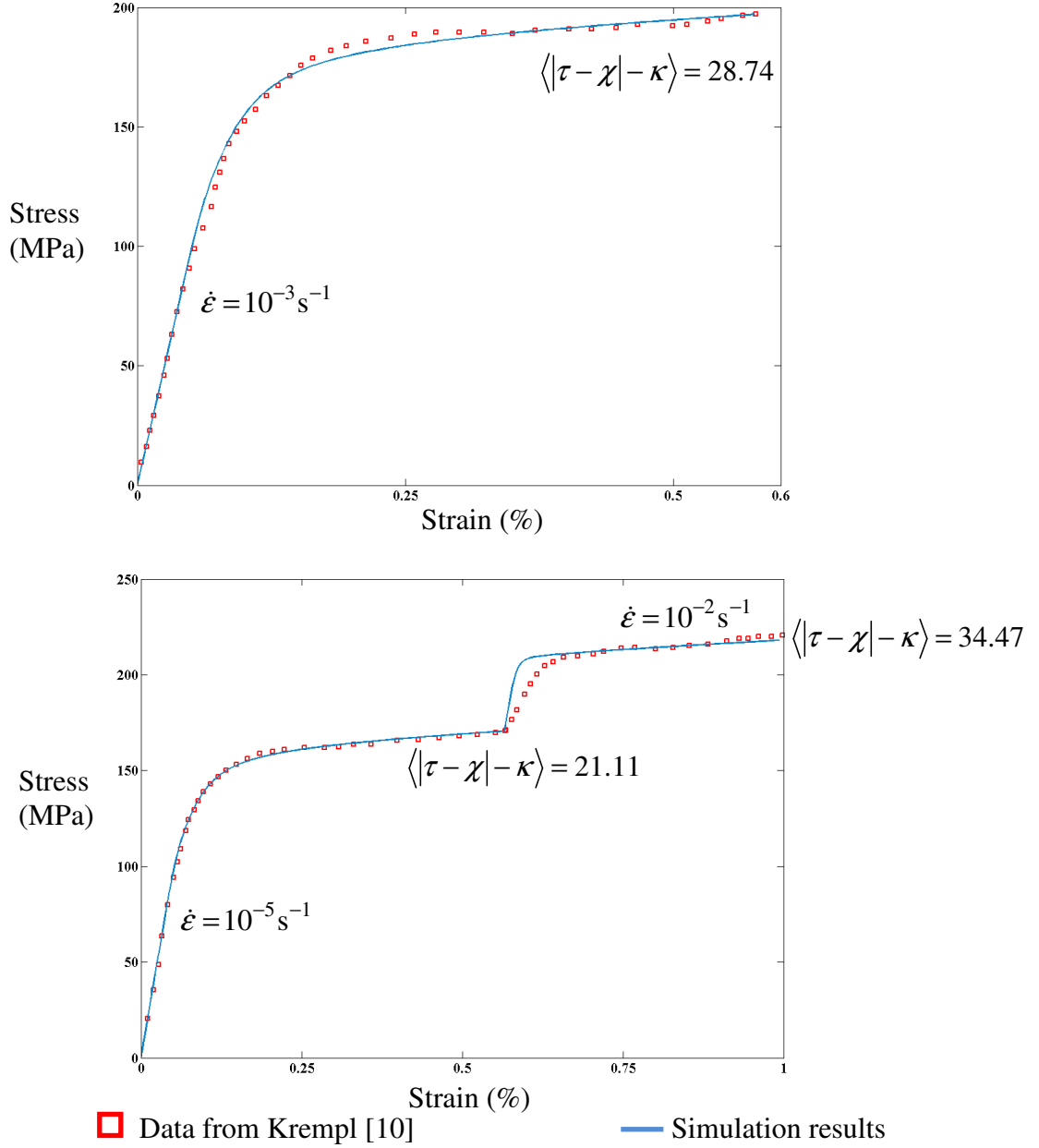
Figure 13: Single strain rate and strain rate jump tests – comparison with experiments.

The anistropic (single crystal) elastic constants [14] are:

$C_{11} = 206$ GPa $\quad C_{12} = 133$ GPa $\quad C_{44} = 119$ GPa

The calibrated crystal plasticity parameters are:

$\dot{\gamma}_0 = 1.0 \times 10^{-4}$ s^{-1}, $\quad m = 14$

$g_0 = 27.5$ MPa; $\quad \kappa_0^\alpha = 20$ MPa

$A_{dir} = 90$ GPa, $\quad A_{dyn} = 5000$

As mentioned earlier, the material hardening evolves as it is loaded cyclically implying that the hardening parameters for stable cyclic hysteresis would be different from the tensile parameters.
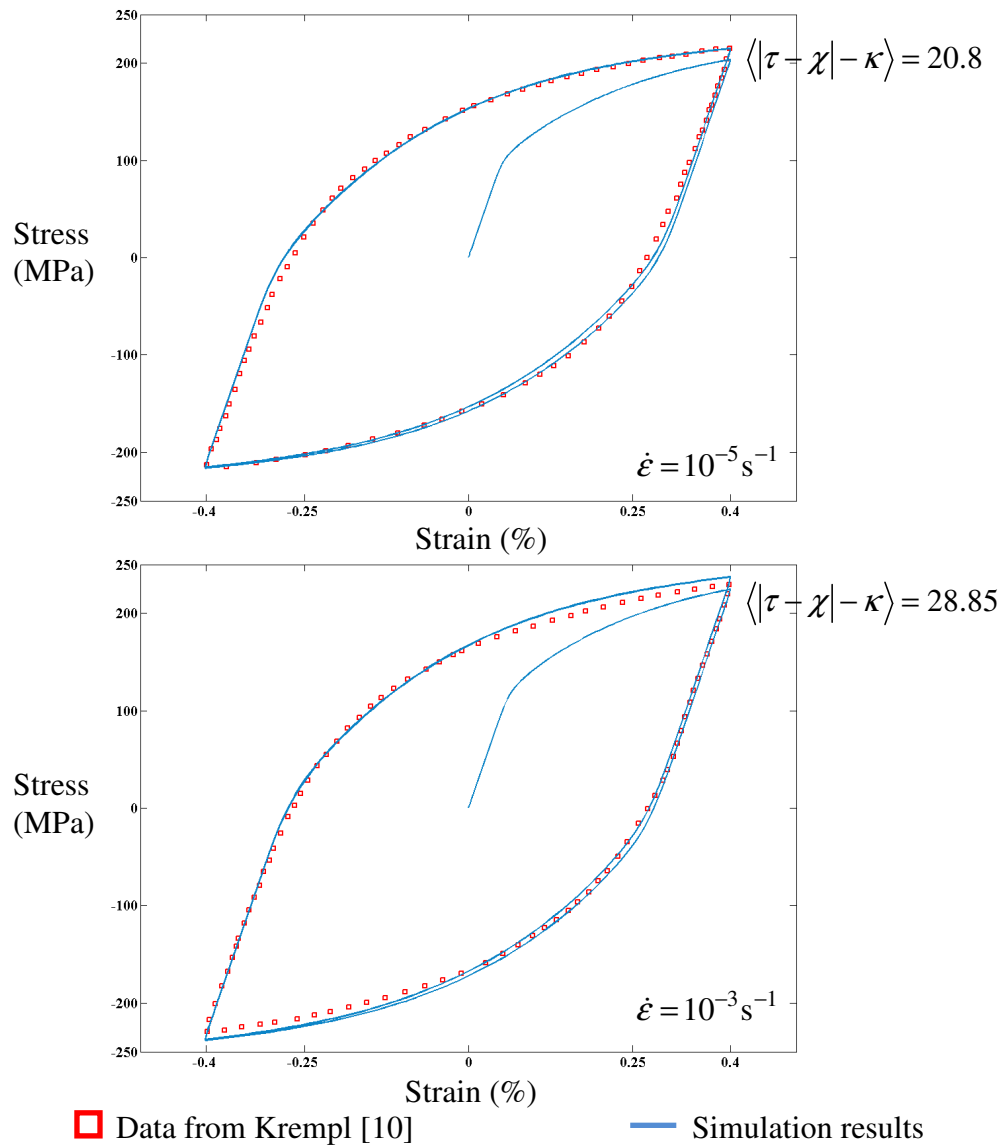
Figure 14: Fully reversed strain controlled tests for three cycles – comparison with experiments.

Completely reversed strain was imposed for three cycles on the same finite element mesh for calibration of crystal plasticity parameters for stabilized hysteresis. The comparison of simulations with experiments is shown in Figure 14. Note that the average overstress values are comparable for the same strain rates for tensile and cyclic loading. The calibrated crystal plasticity parameters are:

$$\dot{\gamma}_0 = 1.0 \times 10^{-4} \text{ s}^{-1}, \quad m = 14$$

$$g_0 = 25.0 \text{ MPa}; \quad \kappa_0^{\alpha} = 20 \text{ MPa}$$

$$A_{dir} = 27.5 \text{ GPa}, \quad A_{dyn} = 650$$

5 Meshing strategies and Microstructure modeling

5.1 Meshing

The numerical means used to solve the boundary value problem is the finite element method (ABAQUS, Simulia, Dassault Systemes, Providence, RI, 2009). The method involves discretizing the domain into contiguous segments and obtaining a solution such that it satisfies the governing differential equation in each finite element and is also continuous over the entire domain.

The problem at hand produces significant gradients of solution fields (strain) at the notch root. This requires that the problem domain be much larger than the notch size and the associated length scale of the gradients of the solution fields. The solution gradients also require that the mesh at the notch root should be fine. To account for the change in the mesh sizes, a domain decomposition approach is taken, as explained in the previous sections, with each domain governed by different constitutive relations and progressively coarsened mesh away from the notch root. The decomposition of the problem domain into different zones is shown in Figure 15 (compare with Fig. 2).
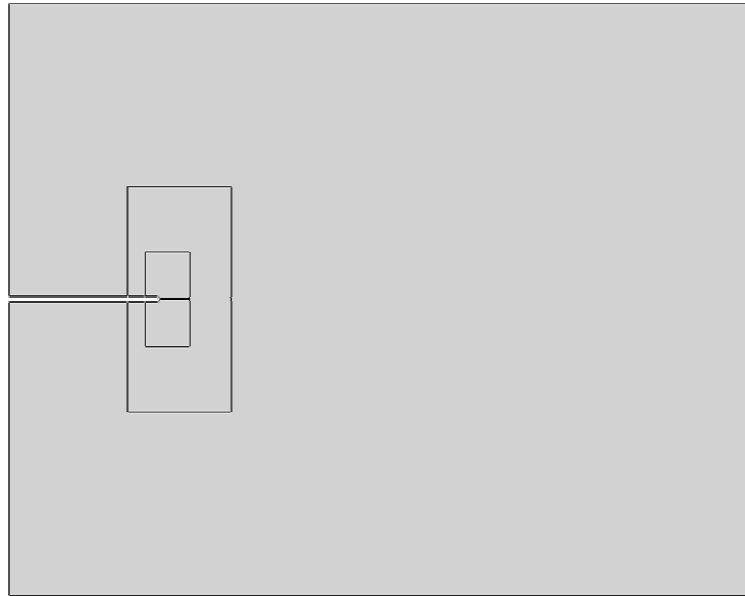

Figure 15: Domain decomposition for the graded finite element mesh.

14

An additional factor that governs the size of the mesh near the notch root is the cutoff length of the mantle (Section 3.2). Prescribing the mesh size to be the same as the cutoff length assures the desired partition of a grain into the mantle and core zones. This yields the size of the finite element in the crystal plasticity zone to be $5\ \mu$m. The meshes in the successive zones (J2 and elastic) are coarsened gradually. An example of the meshing is shown in Figure 16 for a notch depth of 100 mils (2.54 mm) and notch root radius 2 mils (50.8 μm).

(a)   (b)
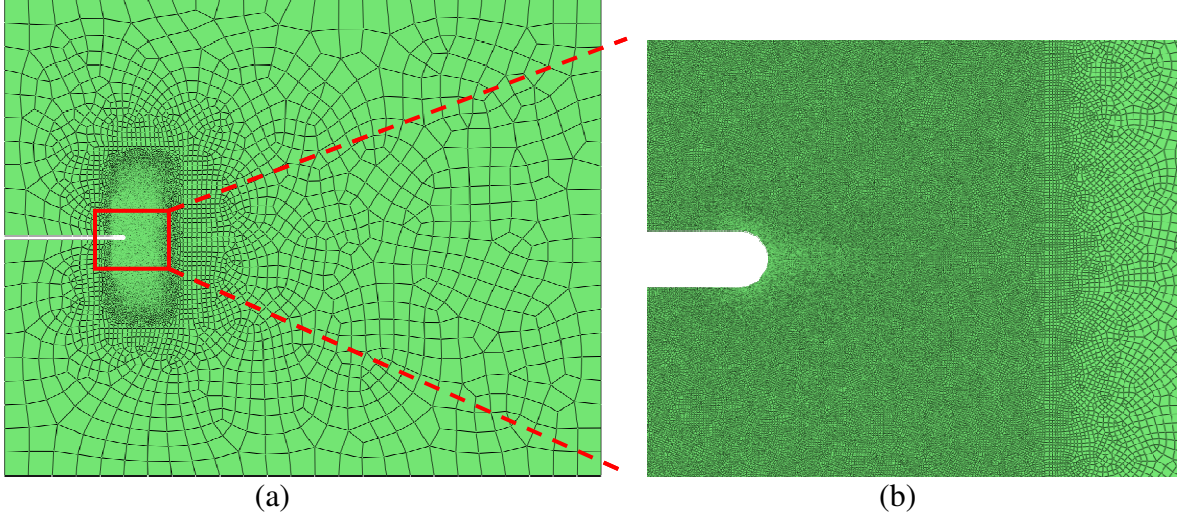
Figure 16: (a) Overall mesh of the domain (115535 Nodes, 116972 Elements) (b) Graded mesh near the notch root.

5.2 Equiaxed grain structure modeling (Wrought microstructure)

The influence of microstructure on the driving force for formation and early growth of fatigue cracks is one of the aspects being explored in this program. Both annealed (wrought) and dendritic microstructures will be investigated. This section details the computational implementation of the microstructure instantiation.

Annealed materials usually display wrought microstructure. The grains do not favor any particular shape, but rather grow into each other. Topologically, the grain structure is very similar to a Voronoi tessellation. However, using a regular Voronoi tessellation to create the microstructure results in grain sizes that fit a normal distribution [15]. Instead, Musinski [15] uses a weighted Voronoi approach in which the weight of individual seeds for the tessellation is described by a log-normal distribution i.e. the logarithm of the grain sizes is normally distributed. The probability density function for the distribution is given by

$$f\left(x,\mu,\sigma\right)=\frac{1}{x\sigma\sqrt{2\pi}}\exp\left(-\frac{\left(\ln x-\mu\right)^2}{2\sigma^2}\right);\quad\left(x>0\right)$$

(7)

where σ and μ are the mean and standard deviation of the natural logarithm of the variable x.

The microstructure generation algorithm has been adopted from Musinski [15] with changes for the applicable geometry and the capability to identify the mantle – core zones of each grain.

15

In the first step, the number of grains is determined based on the total area of the crystal plasticity zone and the average grain size. Characterization studies by QuesTek have revealed that the average grain size is $25\ \mu$m. A log-normal distribution is employed based on the number of grains in the crystal plasticity zone. Here, values of $\mu = 0.4$ and $\sigma = -0.1$ have been assumed. The resulting distribution is the size of the grains normalized by the average size.

Initially, the grains are assumed to be circular, and are arranged in the crystal plasticity zone as shown in Figure 17 (a). The circular packing is achieved by random sequential addition of circles descending from the largest circle – with the constraint that no two circles overlap. It is to be noted that random sequential addition produces a low packing fraction $\left(\approx 0.7\right)$ which is taken into account by scaling down the circle sizes. The resulting packing forms the base on which the equiaxed structure is generated.

The subsequent step involves the identification of finite elements that lie inside a circle. The finite elements that do not explicitly lie inside a circle are assigned to the nearest circle available. In essence, the grain grows to encompass its surrounding area. Once a grain has been formed, the next closest grain is identified. The mid-point of the line joining the surfaces of these two circles forms the grain boundary. The distance of each finite element centroid is calculated from this grain boundary and is identified as belonging to the mantle zone if it is less than the cutoff distance. An example of the circular packing and the resulting microstructure is shown in Figure 17. The mantle and core zones of each grain can be identified in Fig 17 (b). The resulting grain size distribution is compared with the initially prescribed distribution, as shown in Figure 18.

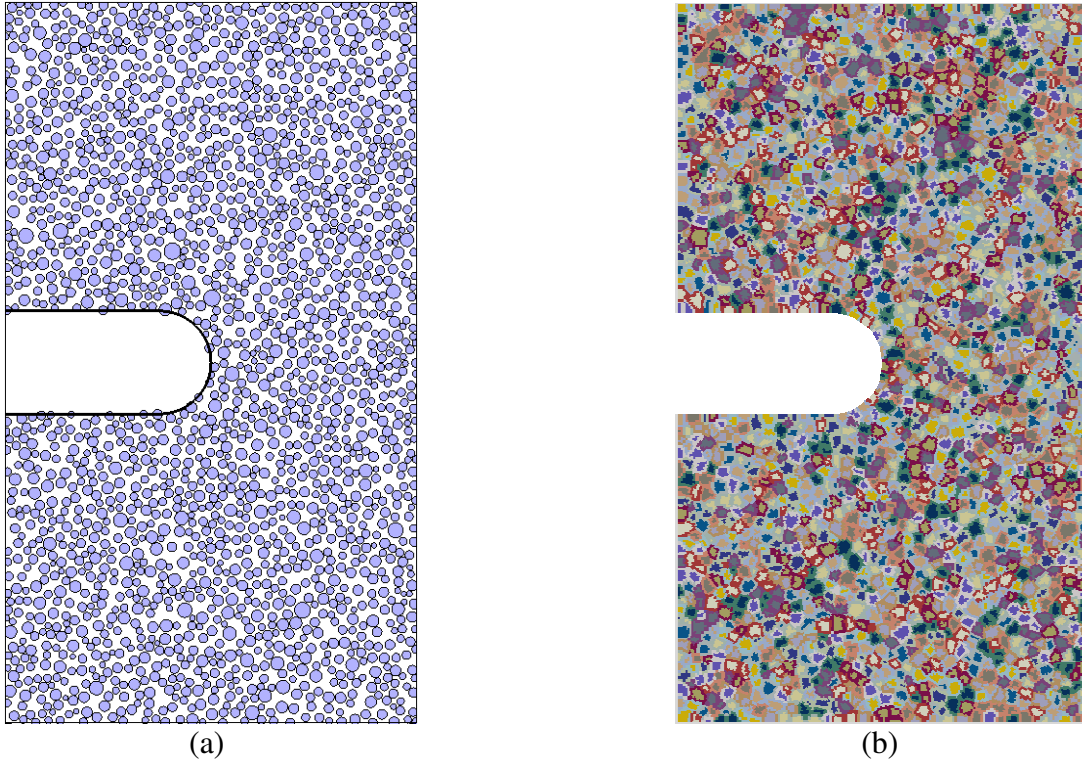(a)   (b)

Figure 17: (a) Circular packing and (b) the resulting equiaxed grain structure derived. (Edges of finite element mesh not plotted for visibility).
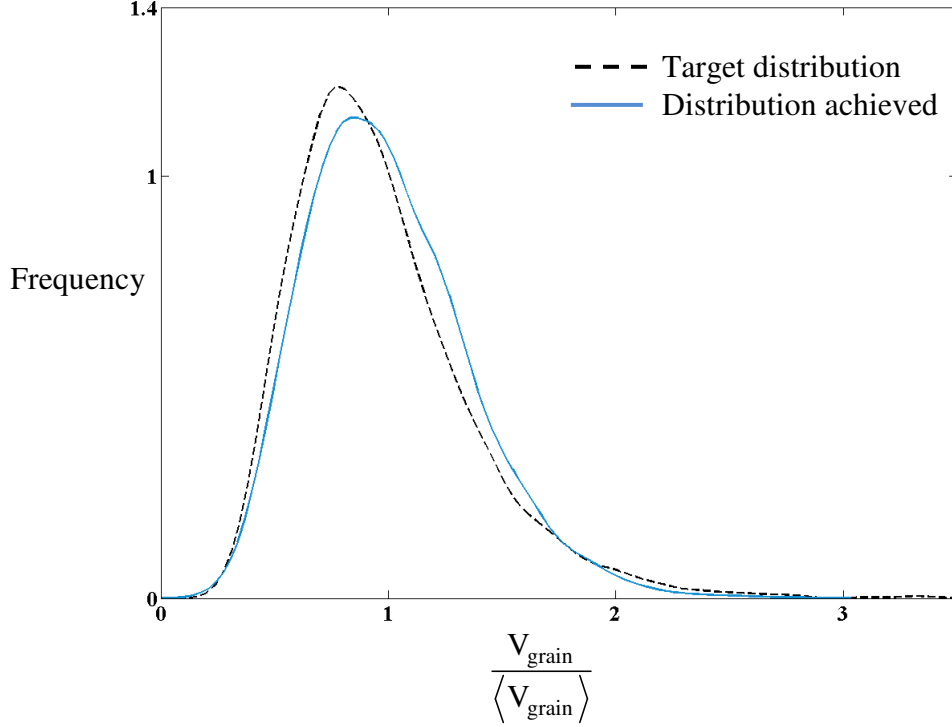
Figure 18: Comparison of the target and achieved grain size distribution for the equiaxed grain structure, normalized by the mean grain volume.

5.3 Dendritic microstructure

The computational procedure for generating dendritic microstructure is outlined here. The creation of the dendritic microstructure differs from the equiaxed structure in only the formation of the base from which the structure is derived – circular packing in the case of equiaxed grains. For a dendritic microstructure a wireframe structure is formed. Each of the dendrites is assumed to have width defined by a log-normal distribution. The initial structure is formed by placing rectangles with equal height, and width defined by the log-normal distribution without overlap. Within each rectangle, wireframe structures are allowed to grow randomly. The result is a random wireframe structure that is spaced according to the size distribution specified. The assignment of finite elements to each dendrite and identification of the mantle – core zones follows the same procedure as for the equiaxed structure with points on the wireframe structure replacing centers of circles packed. The resulting dendritic structure and the associated mantle-core zones are shown in Figure 19(b). The example shown in Fig 19 is for a notch root radius 0.2 mils which is smaller than the average grain size. In such a case, the defect is assumed to have occurred along a grain boundary. This configuration is achieved by constraining that no single grain spans the width of the notch. In cases where the notch root dimensions are larger than the average grain size, such constraints are not necessary.

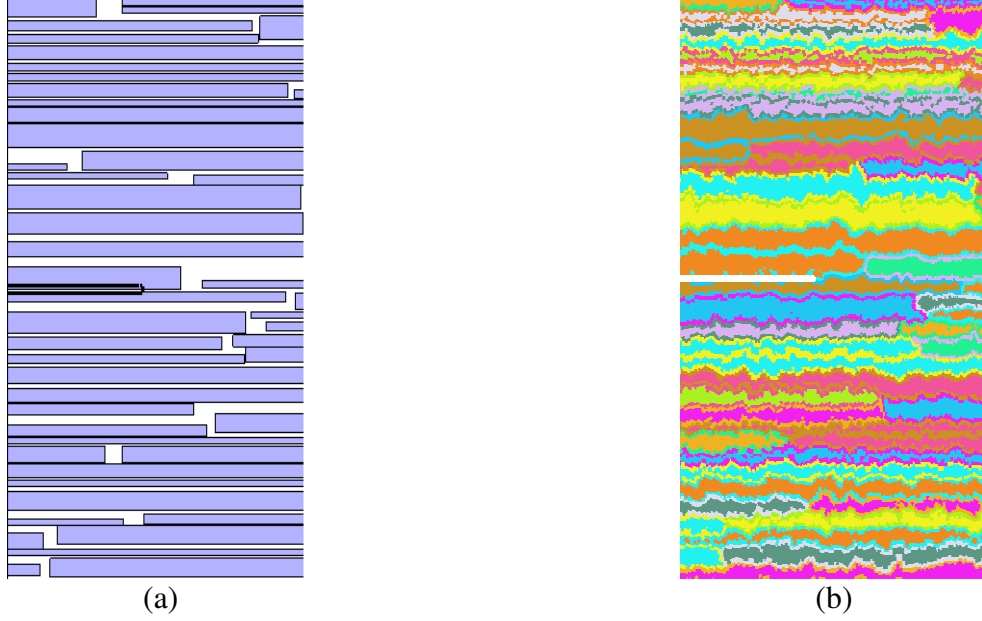(a)   (b)

Figure 19: (a) Initial rectangle packing and (b) the resulting Dendritic grain structure. (Edges of finite element mesh not plotted for visibility).

6 Notch analysis: results

The boundary conditions for the simulation cell are shown in figure 20. The dimensions of the simulation cell are much larger than the dimensions of the notch.
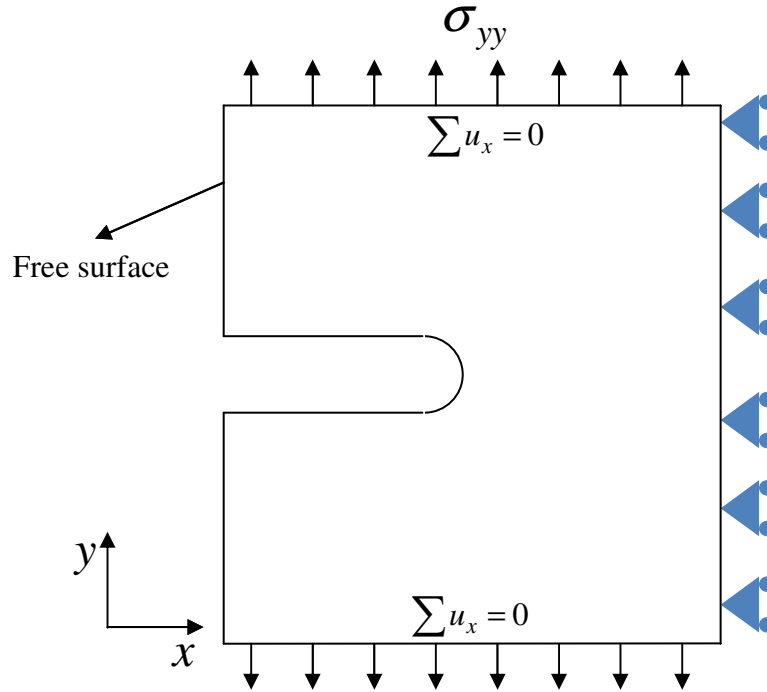

Figure 20: Boundary conditions for the simulation of surface defects.

Detailed parametric simulations considering varying notch root radii were performed. We are presently focusing on dendritic microstructure. The dendritic microstructure is highly textured. The measured texture reported by Hofer [16] and Vendermeulen at al. [14] is used to prescribe the initial orientation of the dendrites. Presently, we assume an orientation distribution that introduces slight misorientation from {100} <110> texture. The distribution of orientations was obtained using a Monte carlo approach which controls the misorientation angle. The average misorientation was -0.15^0 with a standard deviation of 10.2^0 (from QuesTek). An example of the varying microstructure being simulated is shown in figure 19. Typically, four cyclic loading cycles are imposed and the stress distribution at the end of fourth loading cycle is plotted. This is reasonable since cyclically stable hysteresis is achieved with four loading cycles. The stress intensification in the vicinity of the notch root for different R ratios is shown in figure 21. The stresses plotted are the average of the maximum principal stresses within an averaging volume of radius 5 μm. The stresses are averaged at the end of the 4th cycle.
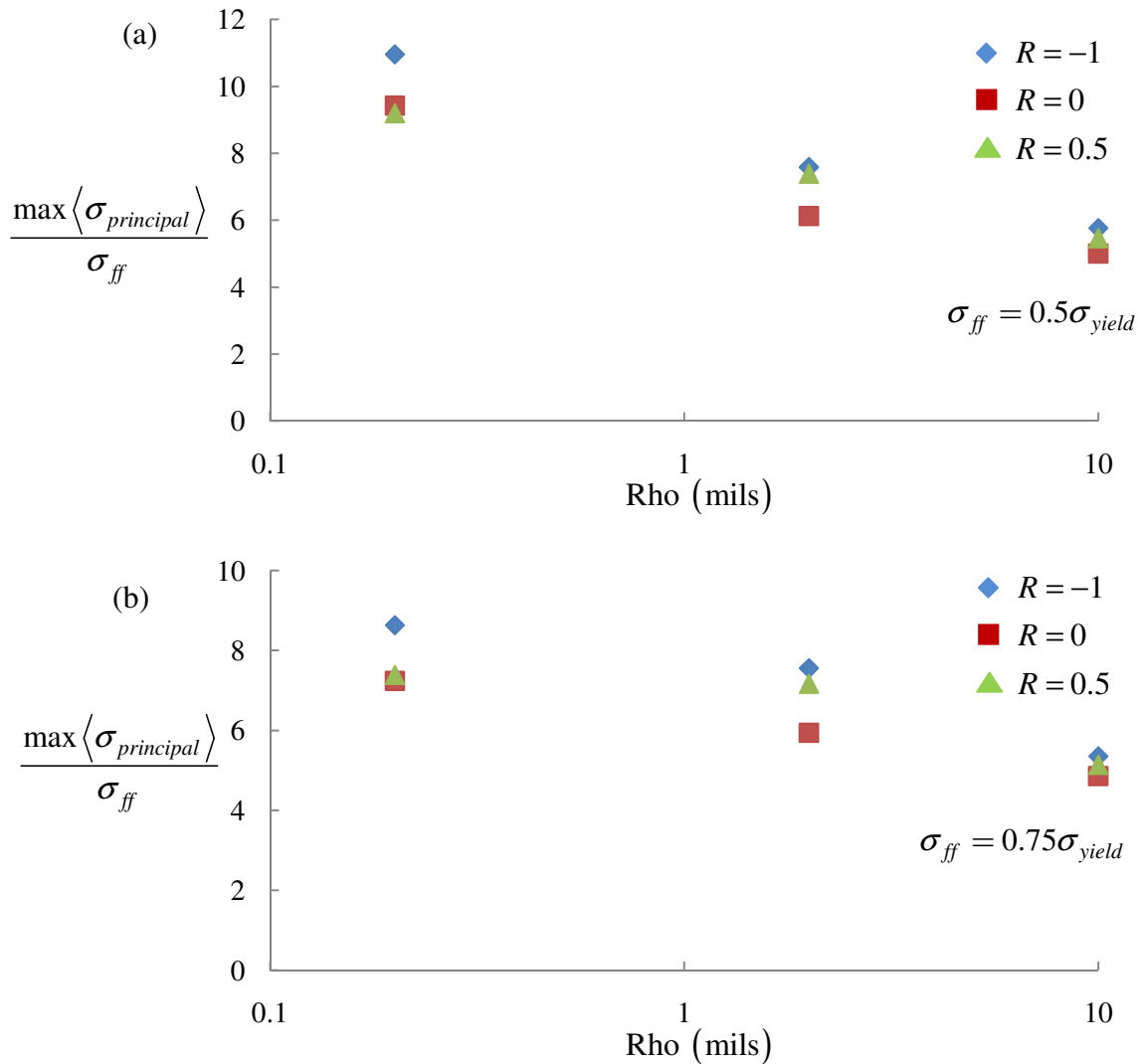

Figure 21: Notch root stress intensification at the end of 4th cycle for an applied remote load of (a) $\sigma_{ff} = 0.5\sigma_{yield}$ and (b) $\sigma_{ff} = 0.75\sigma_{yield}$. The notch depth for all simulations is 100 mils.

The stress intensification is highest for the sharpest notch. Also, the peak stresses are lowest for the case of R = 0 due to the compressive stresses imposed by the surrounding material at the notch root. The observed scatter with respect to the R ratio seems to decrease with the notch root radius for both values of far field stress. This could be due to the dimensions of the notch for a root radius of 10 mils is much larger than the average grain size, thus reducing the variability induced due to the microstructure. The stress – strain history of the same group of elements is plotted in figure 22. The motivation is to compare the macroscopic R ratio to the local R ratio in the vicinity of the notch. Since the remote loading is in the y direction (fig. 20), we plot the corresponding components of the Second Piola-Kirchhoff stress tensor and the Green's strain tensor given by

$$\mathbf{E} = \frac{1}{2}\left(\mathbf{F}^T \cdot \mathbf{F} - \mathbf{I}\right) \tag{8}$$

where $\mathbf{F}$ is the deformation gradient tensor.

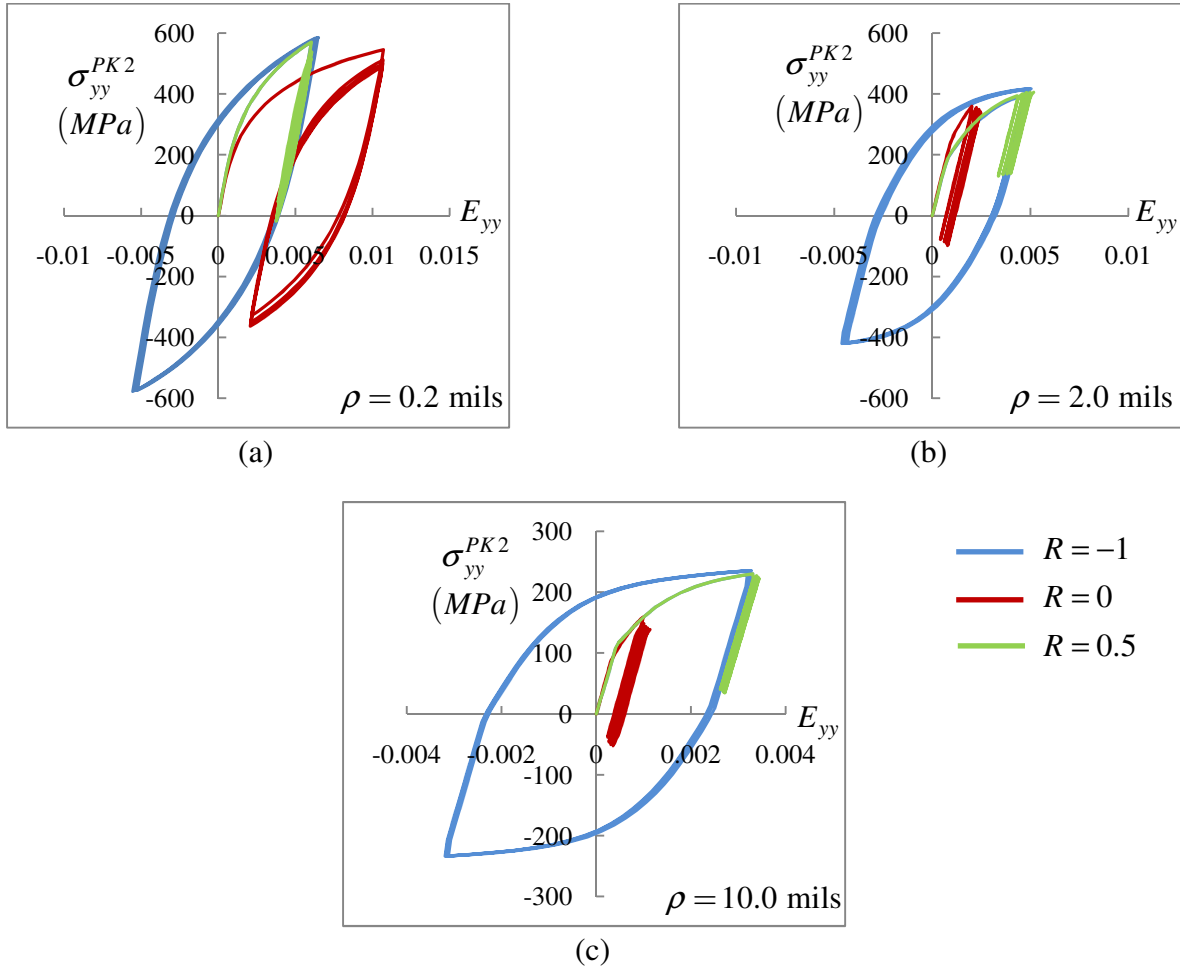Figure 22: Hysteresis loops for local R ratios for remote load $\sigma_{ff} = 0.5\sigma_{yield}$ and notch depth 100 mils and notch root radius of (a) 0.2 mils, (b) 2.0 mils and (c) 10.0 mils.

Note that the identification of these elements is based on the maximum principal stress values at the end of the 4th cycle, which may not be the same elements which have the maximum principal stress at, say, the end of the first cycle. Indeed, this was found to be true in some cases. This indicates that the stress is redistributed with loading cycles indicating that the ratcheting strain plays an important role in this mechanism. The variation between the applied R ratio and the local R ratio seems to decrease with increasing notch root radius. The variation of the cyclic plastic strain range and ratcheting strain with loading conditions and notch geometry is shown in Figure 23.
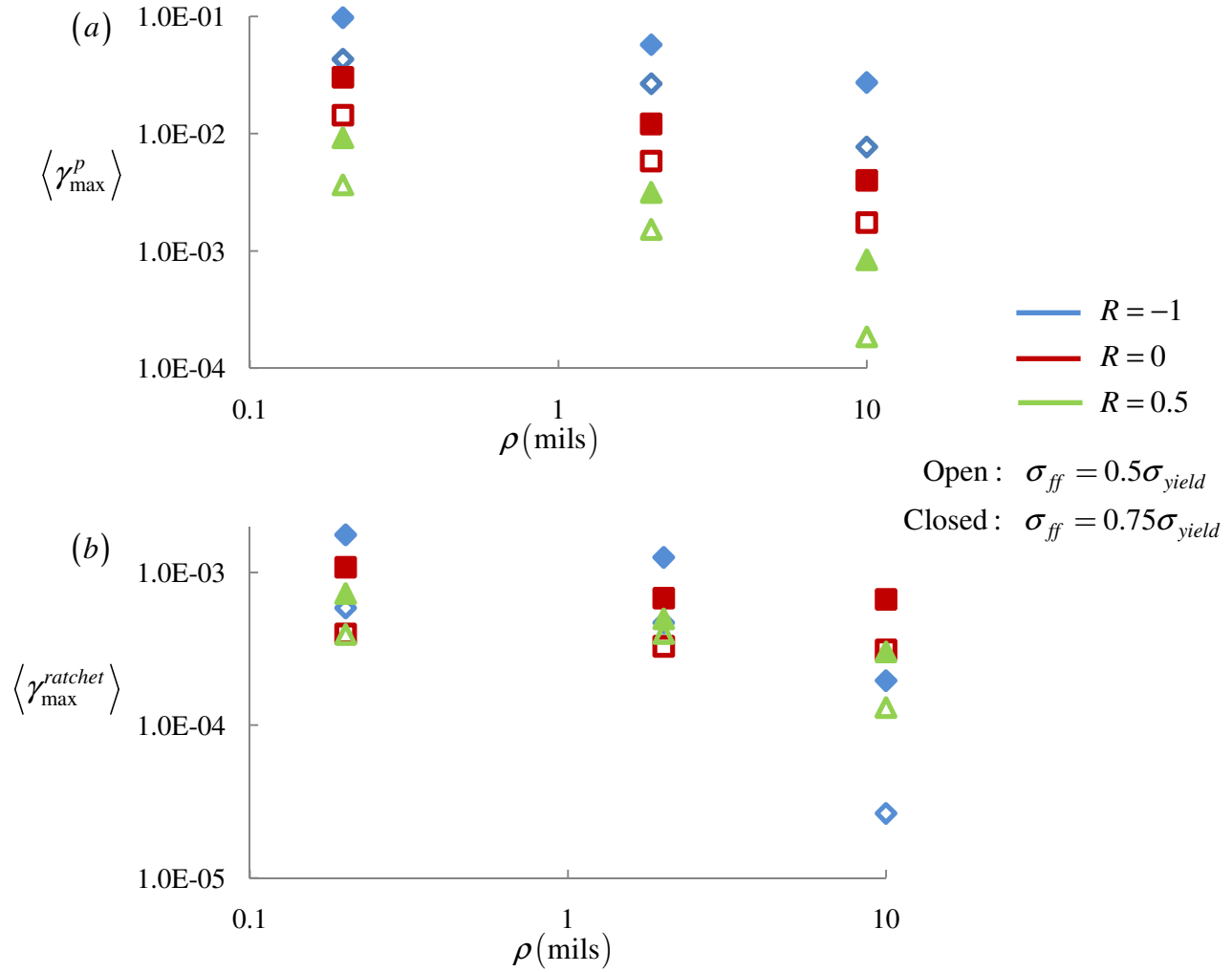

Figure 23: Variation of (a) maximum cyclic plastic strain range and (b) maximum ratcheting strain with remote loading, notch root radius and far field stress. Notch depth is 100 mils.

The maximum cyclic shear strain is observed for the completely reversed loading since it has the largest range of applied stress. The maximum cyclic shear strain varies predictably with the loading conditions with the shear strain range decreasing with increasing R ratio and increasing for increased remote stress amplitude. The ratcheting strain displays a more complex relation with the applied loading conditions. Also, note that for both loading remote stress amplitudes,

the case for R = 0 displays the least variation in ratcheting strain with varying notch root radii. The effect of the intergranular interactions on the slip distribution will need to be investigated.

7. Deliverables

The following codes/scripts have been transferred to QuesTek:

- Python script files for geometric modeling and mesh generation.
- Matlab codes for microstructure generation.
- Matlab codes for preparing the input file for ABAQUS.
- UMAT subroutine for ABAQUS – limited slip implementation.

References

1. Horstemeyer, M. F., McDowell, D. L., and McGinty, R. D., 1999, "Design of Experiments for Constitutive Model Selection: Application to Polycrystal Elastoviscoplasticity," *Modelling and Simulation in Materials Science and Engineering*, Vol. 7, No. 2, pp. 253–273.

2. Bennett, V. P., and McDowell, D. L., 2003, "Polycrystal Orientation Distribution Effects on Microslip in High Cycle Fatigue," *International Journal of Fatigue*, Vol. 25, No. 1, pp. 27–39.

3. Xie, C. L., Ghosh, S., and Groeber, M., 2004, "Modeling Cyclic Deformation of HSLA Steels Using Crystal Plasticity," *Journal of Engineering Materials and Technology*, Vol. 126, ASME, No. 4, pp. 339–352.

4. HKS Inc, ABAQUS User's Manual, v 6.9.

5. Colin, J., Fatemi, A., and Taheri, S., 2010, "Fatigue Behavior of Stainless Steel 304L Including Strain Hardening, Prestraining, and Mean Stress Effects," *Journal of Engineering Materials and Technology*, ASME, Vol. 132, pp. 021008 1-13.

6. Fujita, H., Mori, H., and Inui, H., 1985, "Dislocation behavior in crystals with low stacking fault energy," Proceedings of Yamada conference IX on Dislocations in solids, Ed. Suzuki, H., Ninomiya, T., Sumino, K., and Takeuchi, S., VNU Science Press. pp. 295 - 298.

7. Rho B. S., Hong H. U., and Nam S. W., 2000, "The effect of δ-ferrite on fatigue cracks in 304L steels," *International Journal of Fatigue*, Vol. 22, No. 8, pp. 683-690.

8. Lloyd, J.T, 2010, Implications of Limited Slip In Crystal Plasticity. MS Thesis, Woodruff School of Mechanical Engineering, Georgia Institute of Technology, Atlanta.

9. Hansen N and Ralph B, 1982, "The strain and grain size dependence of the flow stress of copper," *Acta Metallurgica,* Vol. 30, pp. 411-417.

10. Krempl E., 1979, "An experimental study of room-temperature rate-sensitivity, creep and relaxation of AISI type 304 stainless steel," *Journal of the Mechanics and Physics of Solids*, **27**(5-6), pp. 363-375.

11. Kujawski D, Kallianpur V and Krempl E, 1980. "An experimental study of uniaxial creep, cyclic creep and relaxation of AISI type 304 stainless steel at room temperature," *Journal of the Mechanics and Physics of Solids*, **28**(2), pp. 129-148.

12. Moosbrugger JC, 1991, "Some developments in the characterization of material hardening and rate sensitivity for cyclic viscoplasticity models," *International Journal of Plasticity*, Vol. 7, No. 5, pp. 405 – 431.

13. Leax, T.R., 1999, "Statistical Models of Mean Stress and Water Environment Effects on the Fatigue Behavior of 304 Stainless Steel, in Probabilistic and Environmental Aspects of Fracture and Fatigues," PVP Vol. 386, S. Rahman, ed., American Society of Mechanical Engineers, New York, pp. 229–239.

14. Vandermeulen, W., Schibetta, M., Leenaers, A., Schuurmans, J., and Gerard, R., 2008, "Measurement of the Young's Modulus anisotropy of a reactor pressure vessel cladding," *Journal of Nuclear Materials*, Vol. 372, 2008, pp. 249-255.

15. Musinski WD, 2010, Novel Methods for Microstructure-Sensitive Probabilistic Fatigue Notch Factor. MS Thesis, Woodruff School of Mechanical Engineering, Georgia Institute of Technology, Atlanta.

16. Hofer, G., 1988, "Texture Dependent Young's Modulus in Austenitic Cladding," Textures and Microstructures, Gordon and Breach Science Publishers, Inc., UK, Vols. 8&9, pp. 611-617.